Broadband Antireflective Properties of Inverse Motheye Surfaces

Mark S. Mirotznik, *Associate Member, IEEE*, Brandon L. Good, *Member, IEEE*, Paul Ransom, *Member, IEEE*, David Wikner, and Joseph N. Mait, *Senior Member, IEEE*

***Abstract*—A new method for synthesizing broadband antireflective (AR) surfaces at microwave and millimeter wave frequencies is demonstrated. The AR surface, we call an inverse motheye, was formed by machining a multi-layer grating of subwavelength circular holes into a non-absorptive dielectric. This created low reflected energies (< -30 dB) over reasonably large bandwidths and incidence angles. An optimization algorithm, based on a direct pattern search, integrated with a rigorous electromagnetic model was used to design the grating geometries. Experimental results are provided at Ka-band demonstrating the validity of the method.**

***Index Terms*—Antireflection, effective medium, millimeter wave, rigorous couple wave, subwavelength gratings.**

I. INTRODUCTION

RECENT advances in passive imaging at millimeter wave frequencies [1]–[3] have created a need for high quality optical components, such as lenses, designed specifically for these wavelength bands. For most passive millimeter wave imaging applications it is of critical importance to collect as much incoming radiation as possible since signal strengths are commonly many orders of magnitude smaller than intensities encountered at visible or infrared wavelengths. Even at optical wavelengths, however, it is desirable to maximize light collection. To accomplish this, antireflective (AR) coatings are often applied to the surface of passive components, such as lenses, to suppress Fresnel reflections and, as a consequence, collect more energy in the desired waveband. The most common method for implementing broadband AR surfaces is to coat the surface with multiple layers of thin films. Various optimization algorithms are used to determine exact values for the number of layers, dielectric constant and their respective thicknesses such that the coating produces the least amount of reflected energy over the desired spectral band. In general, as the number of layers increases, the antireflective behavior improves. Unfortunately, implementing this same approach at microwave and millimeter wavelengths can be challenging since materials with the desired dielectric constants are scarce. An alternative method, originally developed for designing AR surfaces in visible and infrared applications, utilizes a multi-level subwavelength grating fabricated directly on the surface of a dielectric [4]–[6]. This technique was biologically inspired by the subwavelength surface pattern on the cornea of common insects including many moths and butterflies (see Fig. 1).

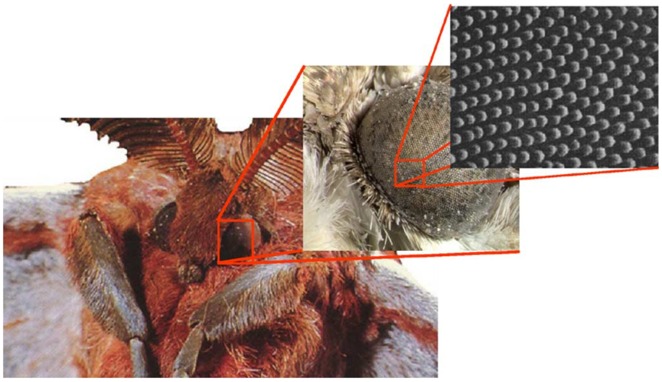

Fig. 1. The corneal surface of many insects is structured with a subwavelength grating of protrusions that are believed to provide wide bandwidth antireflective properties over the optical spectrum.

In fact, these insect's eyes appear completely black due to the AR properties of its subwavelength structure. Consequently, man-made AR surfaces of this type are often called "motheye" surfaces (see Fig. 2). Similar to the conventional thin film AR coatings the performance of motheye AR surfaces improves as the number of levels increases. Unfortunately, most multi-level designs of conventional motheye surfaces result in very thin needle-like structures protruding from the surface of a dielectric. These structures can be difficult to fabricate and often lack the mechanical rigidity required for some applications. In this paper we present an alternative structure, an inverse motheye surface, which can be significantly easier to fabricate than a motheye, is more mechanically robust, and still provides good broadband AR behavior. This new structure, illustrated in Fig. 3, is formed by drilling multi-level subwavelength holes of various diameters into a non-absorptive substrate. Two design algorithms were developed and are presented here. One is a direct design approach based on the effective dielectric properties of the subwavelength hole arrays. The other is an iterative optimization algorithm, based on a direct pattern search, integrated with a rigorous electromagnetic model (rigorous coupled wave algorithm (RCW)).

Manuscript received October 12, 2009; revised February 15, 2010; accepted March 20, 2010. Date of publication June 14, 2010; date of current version September 03, 2010.

M. S. Mirotznik and B. L. Good are with the Electrical and Computer Engineering, University of Delaware, Newark, DE 19716 USA and also with the Carderock Division, Naval Surface Warfare Center, West Bethesda, MD 20817 USA (e-mail: mirotzni@ece.udel.edu; Brandon.good@navy.mil).

P. Ransom is with the Catholic University of America, Washington, DC 20064 USA and also with the Carderock Division, Naval Surface Warfare Center, West Bethesda, MD 20817 USA (e-mail: paul.ransom@navy.mil).

D. Wikner and J. N. Mait are with the U.S. Army Research Laboratory, Adelphi, MD 20783 USA (e-mail: david.wikner@arl.army.mil; jmait@arl.army.mil).

Color versions of one or more of the figures in this paper are available online at http://ieeexplore.ieee.org.

Digital Object Identifier 10.1109/TAP.2010.2052575

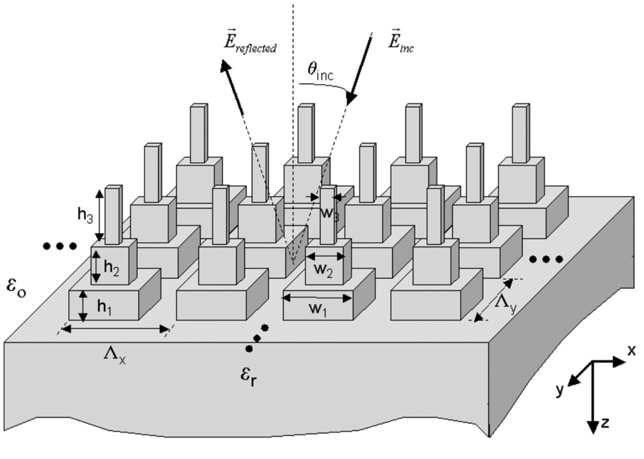

Fig. 2. Illustration of a conventional motheye AR surface.

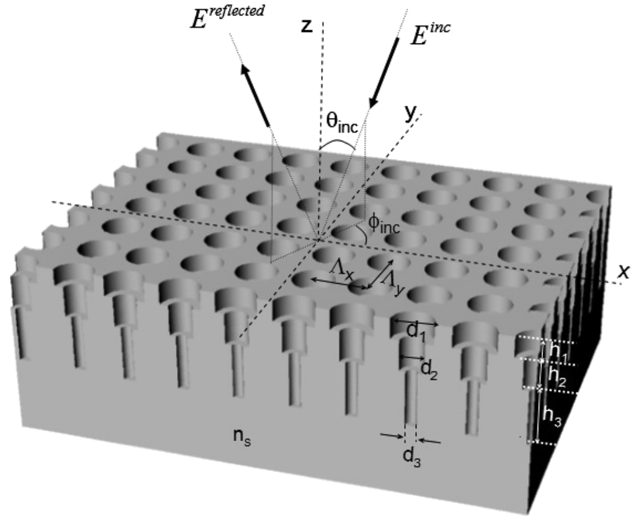

Fig. 3. Illustration of an inverse motheye surface formed by drilling a multi-level pattern of subwavelength holes into a non-absorptive dielectric substrate.

Both methods were used to design inverse motheye AR surfaces within the Ka-band. We validated our design methodologies by fabricating a test sample and characterizing it experimentally.

II. PROBLEM GEOMETRY

Fig. 3 depicts the subwavelength structures that we investigated for use as an AR surface. The gratings were multi-level (three levels shown in the figure) subwavelength holes with circular cross sections. We assumed we could form this surface by drilling holes in a non-absorptive dielectric of permittivity, ε_r, and index of refraction, n_s. To avoid any propagating diffracted orders, other than the zeroth order, the period of the gratings along the x- and y-axes, denoted by Λ_x and Λ_y respectively, should be smaller than the material wavelength. The hole diameter and depth of each layer, denoted by d_n and h_n respectively, were assumed variable and chosen to produce a minimum amount of reflected energy over some desired frequency band and incident angles. In the examples we present in this paper the incident field is restricted to TE polarized plane waves propagating at an angle θ_{inc} with respect to the z-axis (as illustrated in Fig. 3). However, one can apply the algorithm, without modification, to problems involving plane waves of arbitrary incident angles and polarizations. Two variations to the basic design, illustrated in Fig. 3, were also studied. In particular, we considered hexagonally packed hole arrays, as well as structures in which the holes were backfilled with a different material of index of refraction n_h. These alternative geometries are illustrated in Fig. 4.

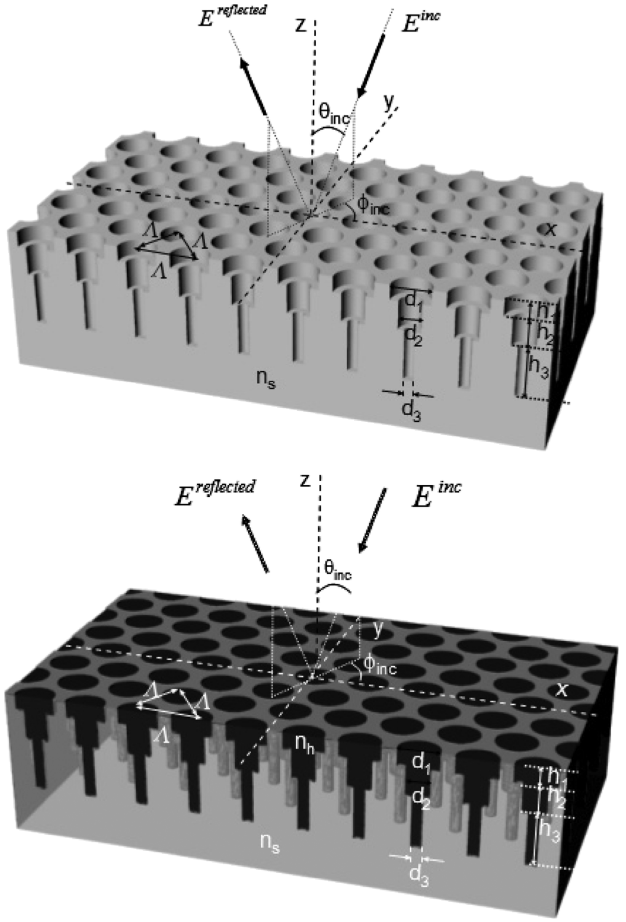

Fig. 4. Variations to the basic inverse motheye design (shown in Fig. 3) includes hexagonally packed array (top) and dielectrically backfilled design (bottom).

III. ELECTROMAGNETIC MODELING

Two approaches are generally reported in the literature for simulating the electromagnetic properties of subwavelength gratings. The first uses effective media theory [7] to provide closed form approximations for the effective dielectric constants as a function of the grating structure. Although attractive from a computational perspective, the approximate expressions are accurate only for gratings whose period is much smaller than the wavelength of illumination. As the grating period approaches the wavelength, which is referred to as the resonance regime, the assumptions on which these closed form expressions are based are no longer valid. For our designs we assumed grating periods only slightly smaller than the material wavelength and thus could not accurately utilize effective media theory.

We employed a second approach, which utilizes a rigorous electromagnetic model to determine the relationship between structural form and response. Although computationally more difficult, this approach is capable of generating accurate results for gratings of any period size and shape. Several rigorous electromagnetic models can be used for this calculation. We chose the rigorous coupled wave (RCW) algorithm originally presented by Moharam and Gaylord [8], [9]. Our specific implementation, is based on the enhanced transmittance matrix approach introduced by Moharam *et al.* [10] and later refined by Lalanne [11] and Noponen and Turunen [12].

Using this method we define regions within the solution domain illustrated in Figs. 3 and 4. These are; (1) *an incident region* which was assumed to be an infinite half-spaced filled with a lossless dielectric of index $\mathrm{n_{inc}}$, (2) *an exit region* which was assumed to be another infinite half-spaced filled with a lossless dielectric of index $\mathrm{n_{exit}}$, and (3) *a layered grating region* which contains multiple layers of dielectric slabs with subwavelength circular holes. The total thickness of the layered region is

$$H_{tot} = \sum_{n=1}^{N} h_n \tag{1}$$

where h_n denotes the thickness of each layer and N denotes the total number of layers. The first step in the RCW method is to represent the electromagnetic fields in each of the three regions.

A. Incident Region

Within the incident region, denoted by region I, the electromagnetic fields consist of an incident plane wave plus all of the diffracted orders reflected from the structure [12]. This is written for the electric fields as

$$\overline{E}_I = \hat{u}\exp(-j\vec{k}_I\cdot\vec{r}) + \sum_{m=-\infty}^{\infty}\sum_{n=-\infty}^{\infty}\vec{R}_{mn}\exp\left(-j(\vec{k}_{I,mn}\cdot\vec{r})\right) \tag{2}$$

where $\vec{k}_I$ and $\hat{u}$ denotes the wave vector and unit polarization vector of the incident plane wave respectively. The second term in (2) accounts for all the reflected diffractive orders. Since each of the components in (2) represent plane waves the magnetic field equations can be easily derived from these. In (2) $\vec{R}_{mn}$ and $\vec{k}_{I,mn}$ denotes the vector reflection coefficient and wave vector of the mn-th reflected order in region I respectively. The vector components of $\vec{k}_{I,mn}$, resulting from the phase matching and Floquet conditions, and are given by

$$\vec{k}_{I,mn} = \hat{u}_x\left[k_o n_{inc}\sin(\theta_{inc})\cos(\phi_{inc}) - \frac{2\pi m}{\Lambda_x}\right] + \hat{u}_y\left[k_o n_{inc}\sin(\theta_{inc})\sin(\phi_{inc}) - \frac{2\pi n}{\Lambda_y}\right] + \hat{u}_z k_{Iz,mn} \tag{3}$$

where θ_{inc} is the polar angle and ϕ_{inc} is the azimuth angle of the incident plane wave [8], [9] and [12]. The z component of the wave vector, given in (3), is written more explicitly in (4), shown at the bottom of page where $k_{x,m}$ and $k_{y,n}$ denotes the x and y component of the wave vector given in (3). It is easily deduced from (3) and (4) that if the grating periods, Λ_x and Λ_y, are small compared to the incident wavelength $(\lambda_\mathrm{o}/\mathrm{n_{inc}})$ only the $(\mathrm{m} = \mathrm{n} = 0)$ diffractive order will propagate in reflection (i.e., all other diffractive orders will be evanescent). This condition is written mathematically as

$$\begin{aligned}\Lambda_x &< \frac{\lambda_o}{n_{inc}\left(1-\sin(\theta_{inc})\cos(\phi_{inc})\right)}\\ \Lambda_y &< \frac{\lambda_o}{n_{inc}\left(1-\sin(\theta_{inc})\sin(\phi_{inc})\right).}\end{aligned} \tag{5}$$

In this work we are interested in generating only zeroth order AR surfaces thus the conditions given by (5) must be enforced.

B. Exit Region

Within the exit region, denoted by region III, the electromagnetic fields consist all of the diffracted orders transmitted through the structure [12]. This is written for the electric fields as

$$\overline{E}_{III} = \sum_{m=-\infty}^{\infty}\sum_{n=-\infty}^{\infty}\vec{T}_{mn}\exp\left(-j(\vec{k}_{III,mn}\cdot\vec{r})\right) \tag{6}$$

Here $\vec{T}_{mn}$ and $\vec{k}_{III,mn}$ denotes the vector transmission coefficient and wave vector of the mnth transmitted order in region III respectively. The wave vector in region III is of the same mathematical form as (3) and (4) in region I with the one exception of replacing $\mathrm{n_{inc}}$ with $\mathrm{n_{exit}}$. Using a similar analysis to that of region I it can easily be shown that to avoid any propagating diffractive orders in the transmitted region, other than the $\mathrm{m} = \mathrm{n} = 0$ term, the grating periods must satisfy the relations

$$\begin{aligned}\Lambda_x &< \frac{\lambda_o}{n_{exit}\left(1-\sin(\theta_{inc})\cos(\phi_{inc})\right)}\\ \Lambda_y &< \frac{\lambda_o}{n_{exit}\left(1-\sin(\theta_{inc})\sin(\phi_{inc})\right).}\end{aligned} \tag{7}$$

C. Multi-Layered Grating Region

Between the incident and exit regions is a multi-layered stack of N grating layers, denoted as region II. Each of the layers within region II is assumed to be of finite thickness and contains an array of subwavelength circular holes drilled out of a dielectric substrate (illustrated in Fig. 5). Both rectangular and hexagonally packed hole arrays were investigated.

$$k_{zI,mn} = \begin{cases} \sqrt{(n_{inc}k_o)^2 - k_{x,m}^2 - k_{y,n}^2} & k_{x,m}^2 + k_{y,n}^2 < (n_{inc}k_o)^2 \\ -j\sqrt{k_{x,m}^2 + k_{y,n}^2 - (n_{inc}k_o)^2} & k_{x,m}^2 + k_{y,n}^2 > (n_{inc}k_o)^2 \end{cases} \tag{4}$$

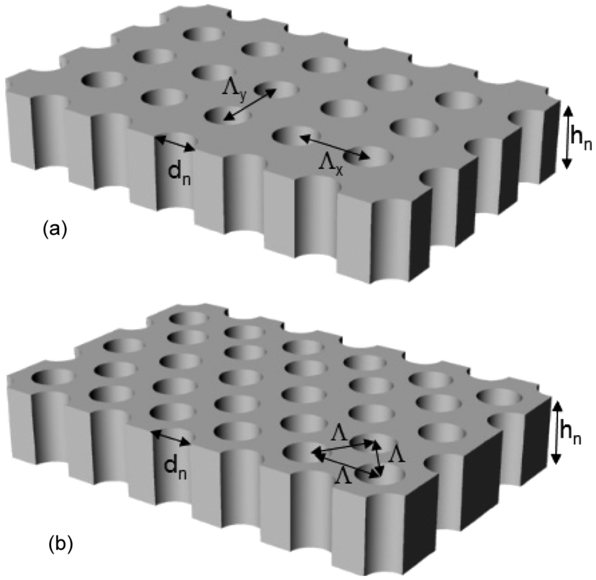

Fig. 5. Each layer within the grating region is assumed to be composed of a periodic lattice of holes whose cross section is independent of depth. In (a) the holes are packed in a rectangular array and in (b) the holes are packed in a hexagonal array.

In the RCW method the electric and magnetic fields within the each layer of the grating region, denoted by the superscript p, are written as a Fourier expansion of spatial harmonics given by

$$\begin{aligned}\vec{E}^p_{II} &= \sum_{m=-\infty}^{\infty}\sum_{n=-\infty}^{\infty} \vec{S}^p_{mn}(z)\exp\left(-j(k_{xm}x+k_{yn}y)\right)\\ \vec{H}^p_{II} &= -j\sqrt{\frac{\varepsilon_o}{\mu_o}}\sum_{m=-\infty}^{\infty}\sum_{n=-\infty}^{\infty}\vec{U}^p_{mn}(z)\\ &\quad\times\exp\left(-j(k_{xm}x+k_{yn}y)\right) \qquad (8)\end{aligned}$$

where $\vec{U}^p_{mn}(z)$ and $\vec{S}^p_{mn}(z)$ represent the amplitudes of the spatial harmonics in the pth layer for the magnetic and electric fields respectively [12]. Substituting (8) into Maxwell's two curl equations and eliminating the z component results in the following coupled system of first order differential equations for the spatial harmonic amplitudes of (8)

$$\begin{aligned}\frac{\partial S^p_{ymn}(z)}{\partial z} &= U^p_{xmn}(z) + \frac{k_{yn}}{k_o^2}\sum_{q=-\infty}^{\infty}\sum_{r=-\infty}^{\infty}\xi^p_{m-r,n-q}\\ &\quad\times\left(-k_{yq}U^p_{xrq}+k_{xr}U^p_{yrq}\right)\\ \frac{\partial S^p_{xmn}(z)}{\partial z} &= -U^p_{ymn}(z) + \frac{k_{xm}}{k_o^2}\sum_{q=-\infty}^{\infty}\sum_{r=-\infty}^{\infty}\xi^p_{m-r,n-q}\\ &\quad\times\left(-k_{yq}U^p_{xrq}+k_{xr}U^p_{yrq}\right)\\ \frac{\partial U^p_{ymn}(z)}{\partial z} &= \sum_{q=-\infty}^{\infty}\sum_{r=-\infty}^{\infty}\varepsilon^p_{m-r,n-q}S^p_{xrq}\\ &\quad+\frac{k_{ym}}{k_o^2}\left(k_{xm}S^p_{ymn}-k_{yn}S^p_{xmn}\right)\\ \frac{\partial U^p_{xmn}(z)}{\partial z} &= -\sum_{q=-\infty}^{\infty}\sum_{r=-\infty}^{\infty}\varepsilon^p_{m-r,n-q}S^p_{yrq}\\ &\quad+\frac{k_{xm}}{k_o^2}\left(k_{xm}S^p_{ymn}-k_{yn}S^p_{xmn}\right) \qquad (9)\end{aligned}$$

In (9), $\varepsilon^p_{m,n}$ and $\xi^p_{m,n}$ denote the Fourier components for the permittivity distribution, $\varepsilon^p(x,y)$, and the inverse permittivity distribution, $1/\varepsilon^p(x,y)$ of the pth layer given by

$$\begin{aligned}\varepsilon^p_{m,n} &= \frac{1}{\Lambda_x\Lambda_y}\int_0^{\Lambda_x}\int_0^{\Lambda_y}\varepsilon^p(x,y)\\ &\qquad\times\exp\left(-j\left(\frac{2\pi mx}{\Lambda_x}+\frac{2\pi ny}{\Lambda_y}\right)\right)dxdy\\ \xi^p_{m,n} &= \frac{1}{\Lambda_x\Lambda_y}\int_0^{\Lambda_x}\int_0^{\Lambda_y}\frac{1}{\varepsilon^p(x,y)}\\ &\qquad\times\exp\left(-j\left(\frac{2\pi mx}{\Lambda_x}+\frac{2\pi ny}{\Lambda_y}\right)\right)dxdy. \qquad (10)\end{aligned}$$

For the geometries of interest here, shown in Fig. 5, (10) can be solved analytically. For the rectangular array, shown in Fig. 5(a), the solution to (10) is given by

$$\begin{aligned}\varepsilon^p_{m,n} &= \frac{d_p\left(\varepsilon^p_s-\varepsilon^p_h\right)}{2\Lambda_x\Lambda_y}\frac{J_1\left(\pi d_p\sqrt{\left(\frac{m}{\Lambda_x}\right)^2+\left(\frac{n}{\Lambda_y}\right)^2}\right)}{\sqrt{\left(\frac{m}{\Lambda_x}\right)^2+\left(\frac{n}{\Lambda_y}\right)^2}}\\ \xi^p_{m,n} &= \frac{d_p\left(\frac{1}{\varepsilon^p_s}-\frac{1}{\varepsilon^p_h}\right)}{2\Lambda_x\Lambda_y}\frac{J_1\left(\pi d_p\sqrt{\left(\frac{m}{\Lambda_x}\right)^2+\left(\frac{n}{\Lambda_y}\right)^2}\right)}{\sqrt{\left(\frac{m}{\Lambda_x}\right)^2+\left(\frac{n}{\Lambda_y}\right)^2}} \qquad (11)\end{aligned}$$

where J_1 denotes the Bessel function of the first kind of order one, d_p represents the diameter of the circular holes within the pth layer and ε^p_s and ε^p_h are the permittivity of the substrate and hole material of the pth layer respectively. For many applications ε^p_h is assumed equal to free-space (i.e., unfilled holes) but could be backfilled with some other material to form a solid flat surface.

If the holes are packed in a hexagonal array, as depicted in Fig. 5(b), the solution to (10) is given by

$$\begin{aligned}\varepsilon^p_{m,n} &= \frac{d_p\left(\varepsilon^p_s-\varepsilon^p_h\right)}{2\sqrt{3}\Lambda}\left(1+\cos\left(\pi(m+n)\right)\right)\\ &\quad\times\frac{J_1\left(\frac{\pi d_p}{\Lambda}\sqrt{\frac{n^2}{3}+m^2}\right)}{\sqrt{\frac{n^2}{3}+m^2}}\\ \xi^p_{m,n} &= \frac{d_p\left(\frac{1}{\varepsilon^p_s}-\frac{1}{\varepsilon^p_h}\right)}{2\sqrt{3}\Lambda}\left(1+\cos\left(\pi(m+n)\right)\right)\\ &\quad\times\frac{J_1\left(\frac{\pi d_p}{\Lambda}\sqrt{\frac{n^2}{3}+m^2}\right)}{\sqrt{\frac{n^2}{3}+m^2}}. \qquad (12)\end{aligned}$$

After substituting (11) or (12) into (9) and enforcing boundary conditions across all planar interfaces an eigenvalue problem results that can be solved numerically for the reflected and transmitted diffracted orders $\vec{R}_{mn}$ and $\vec{T}_{mn}$. For a more detailed description of the numerical implementation of RCW the reader is

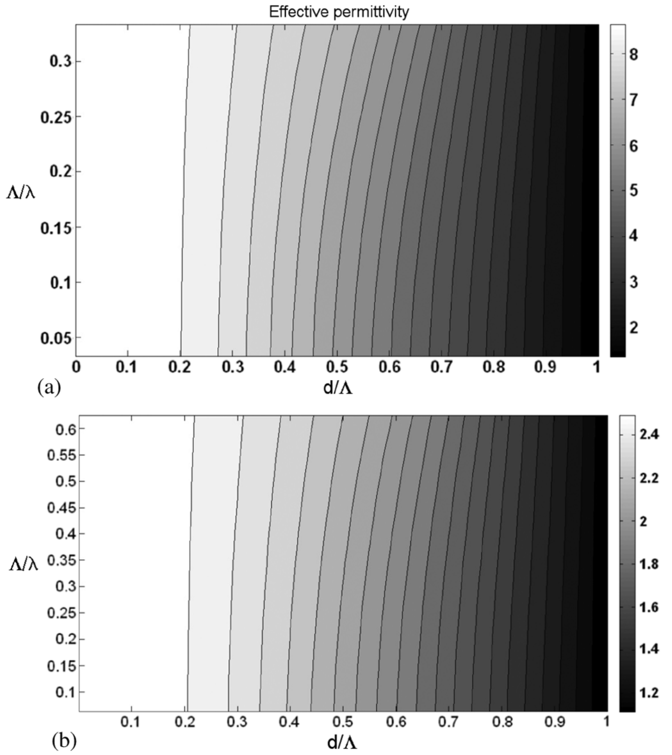

Fig. 6. Effective permittivity of the subwavelength hexagonally packed hole array, depicted in Fig. 5(b), as a function of the periodicity normalized to the free space wavelength (Λ/λ) and the hole diameter normalized to the period (d/Λ). In (a) the substrate was assumed to be a homogenous dielectric slab of dielectric constant $\varepsilon_{\mathrm{r}} = 9.0$ and thickness $\lambda_{\mathrm{o}}/2$ (b) the substrate was assumed to be a homogenous dielectric slab of dielectric constant $\varepsilon_{\mathrm{r}} = 2.56$ and thickness $\lambda_{\mathrm{o}}/2$.

referred to [10]–[12]. Our custom RCW code, developed using the Matlab programming environment, was used to calculate the complex transmission and reflection coefficients from multi-level two-dimensional subwavelength gratings.

IV. Effective Dielectric Constant

The effective properties of the subwavelength geometry illustrated in Fig. 5 can be estimated using the RCW method described in the previous sections. The effective properties are determined by first calculating the zeroth order reflection coefficient, $\mathrm{r_o} = \mathrm{R}_{00}$ as a function of the grating's geometry (i.e. Λ, h and d). The effective permittivity, denoted by $\varepsilon_{\mathrm{eff}}$, can then be determined by solving the transcendental equation

$$r_{input}=\sqrt{\varepsilon_{eff}}\frac{\left(\sqrt{\varepsilon_{inc}}+j\sqrt{\varepsilon_{eff}}\tan\left(\frac{2\pi f}{c}\sqrt{\varepsilon_{eff}}h\right)\right)}{\left(\sqrt{\varepsilon_{eff}}+j\sqrt{\varepsilon_{exit}}\tan\left(\frac{2\pi f}{c}\sqrt{\varepsilon_{eff}}h\right)\right)} \qquad (13)$$

where $\mathrm{r_{input}}$ is given by

$$r_{input} = \sqrt{\varepsilon_{inc}}\frac{1-r_0}{1+r_0}.$$

Fig. 6 illustrates a typical effective permittivity distribution of a hexagonally packed hole array, depicted in Fig. 5(b), as a function of the periodicity of the array normalized to the free space wavelength (Λ/λ) and the hole diameter normalized to the period (d/Λ). The dielectric constant of the incident and exit regions are assumed to be 1.0 while the dielectric constant of the substrate is $\varepsilon_{\mathrm{r}} = 9.0$ in Fig. 6(a) and $\varepsilon_{\mathrm{r}} = 2.56$ in Fig. 6(b). For both Fig. 6(a) and (b) the slab thickness was assumed to be one half the free space wavelength $(\mathrm{h} = \lambda_{\mathrm{o}}/2)$. It is interesting to note that in Fig. 6 as long as the period of the hole array is small compared to the material wavelength (i.e., $\Lambda < \lambda_{\mathrm{o}}/\mathrm{n_s}$) the most sensitive design parameter is the ratio of the hole diameter to the array period (i.e. d/Λ).

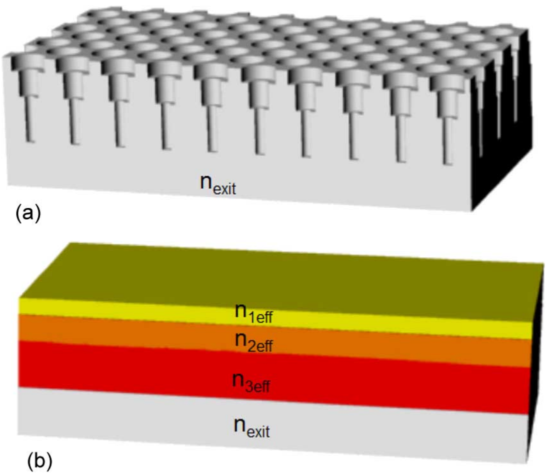

Fig. 7. The multi-level subwavelength grating shown in (a) is approximated by an antireflective interference filter shown in (b). The ERAR algorithm was used to determine the effective properties and thickness of each layer.

V. Design Methodologies

A. *Direct Design of Inverse Motheye Antireflective Surfaces Using Effective Chebyshev Quarter Wavelength Transformers*

In this section we present a direct method of designing inverse motheye surfaces by mapping the "effective" properties of the subwavelength structure to the dielectric properties of a multi-layered dielectric stack. The first step was to employ conventional AR coating design algorithms to construct an interference filter [Fig. 7(b)]. While there are a large number of good algorithms for designing antireflective interference filters we chose to implement the equal ripple algorithm (ERAR) originally described by Collin [11]–[14]. In Collin's method each layer of a multilayered dielectric stack is designed to be of quarter wavelength phase thickness at the center frequency, $\mathrm{f_o}$, of the band of interest (i.e., $\phi(\mathrm{f_o}) = 90^\circ$). Under these conditions the reflectance R(f), as a function of frequency f, for a stack of M layers can be written in the following polynomial form:

$$R(f)=1-\frac{1}{c_o\cos^{2M}(\phi(f))+c_1\cos^{2-1}(\phi(f))+\ldots+c_{2M}} \qquad (14)$$

where, the coefficients, $\mathrm{c_i}$, will depend on the refractive indices, $\mathrm{n_i}$, of each layer. By properly selecting the refractive indices a reflectance function can be derived with desirable antireflective characteristics. Due to their equal ripple character the Chebyshev polynomials are a particularly attractive choice. Fitting (14) to Chebyshev polynomials Collin's derived equations for the refractive indices given the total number of layers M, and desired fractional bandwidth, $\Delta f/f_o$. While Collin only derived equations up to four layers, Riblet [11] presented a recursive algorithm that could be used to determine ni for an arbitrary

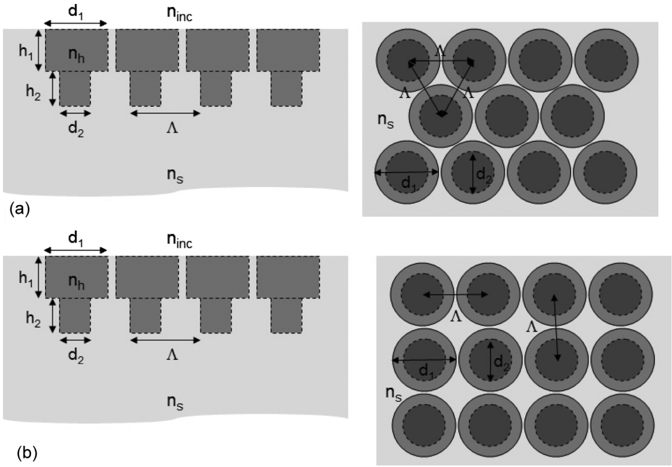

Fig. 8. Inverse motheye AR surface designs described in Example #1 using both the direct effective medium based design algorithm and the iterative optimization. The dielectric constant of the substrate material is $\varepsilon_{\rm r} = 2.56$ Shown are the geometry for a hexagonally packed hole array (a) and for a rectangular packed hole array (b).

number of layers. The mathematical details of the Collin/Riblet algorithm are described in numerous references and for the sake of brevity are not presented here.

The next step was to construct a multi-layered subwavelength grating in which each layer had the same thickness and "effective" refractive indices as the multi-layered design found via Collin's method. We then assumed that when single level subwavelength gratings are stacked to produce a multi-level structure the effective properties of each level could be approximated by the effective properties of the single layer. The authors fully acknowledge that this is an approximation to the true multi-layered structure [Fig. 7(b)], however, as illustrated later by examples, this direct design method did provide reasonably good results. Most often, however, the designs generated by this direct method provided excellent initial conditions for the iterative optimization algorithm described in the next section.

B. Iterative Design Algorithm Using Pattern Search Optimization

To refine the solution of the direct design method we implemented an iterative optimization algorithm. Here the RCW method is used to calculate the full wave solution for the reflected energy of any specific grating structure as a function of frequency and angle of incidence. An optimization algorithm is then used to refine the grating geometry such that an objective function is minimized. The objective function we chose to minimize was simply the sum of squared reflection coefficients, r, at a discrete number of frequencies within the band of interest, $f_{\rm i}$, and a discrete number of angles of incidence, $\theta_{\rm j}$, as given by (15)

$$F = \min\left[\sum_{j=1}^{M}\sum_{i=1}^{N}|r(f_i,\theta_j)|^2\right]. \tag{15}$$

A number of iterative optimization algorithms could be employed to refine the Chebyshev quarter wavelength transformer based designs discussed in the previous section. These include traditional derivative-based algorithms, genetic algorithms or direct pattern search algorithms. An advantage of both genetic and pattern search algorithms is that they do not require derivatives, and so they work well on non-differentiable, stochastic, and discontinuous objective functions. Both simple genetic algorithms and direct pattern search algorithms were implemented and tested for the application of interest here. While both methods produced comparable results the pattern search algorithm was often computationally less expensive. However, the authors fully acknowledge that a comprehensive comparison of the two methods was not conducted.

Pattern search works by searching, or polling, a set of points called a mesh, which expands or shrinks depending on whether any point within the mesh has a lower objective function value than the current point. The mesh size can be expanded or contracted about the current point by adjusting a scaling parameter. If the algorithm finds a point within the mesh whose objective function is less than the current point then that is called a successful poll. After a successful poll, the algorithm moves the current point to the new location and then multiplies the current mesh by a scaling factor greater than one (i.e., expands the mesh). If, however, the poll is unsuccessful then the current point is retained and the algorithm multiplies the current mesh by a scaling factor less than one (i.e., contracts the mesh). The search can be stopped after a minimum pattern size is reached, a maximum number of iterations is exceeded, or the minimum distance between the current points at two consecutive iterations is achieved in the equation at bottom of the following page.

In the next section, we present several examples of AR surfaces designed using both the direct and iterative design methods.

VI. DESIGN EXAMPLES

A. Example #1: Ka-Band (30–40 GHz) Normal Incidence

In this first example an inverse motheye AR surface was designed to reflect a minimum amount of energy within the Ka-band (30–40 GHz) at normal incidence. We assumed that the substrate in which the AR surface would be formed had a dielectric constant of $\varepsilon_{\rm r} = 2.56$ and was infinitely thick (i.e., half-space). For this example we investigated both rectangular and hexagonal arrays.

Hexagonal Hole Array: Implementing both the direct and iterative design approaches described in the previous sections we synthesized a two level AR inverse motheye surface, depicted in Fig. 8(a), using hexagonally packed hole arrays. The grating period, Λ, was fixed at 3.1 mm but the grating heights, ($\rm h_1$ and $\rm h_2$), and hole diameters, ($\rm d_1$ and $\rm d_2$), were assumed variable. Shown in Fig. 8 are the geometrical design results after applying the direct and optimized design approaches.

Rectangular Hole Array: We also designed inverse motheye surfaces composed of subwavelength hole arrays packed in a rectangular configuration, as shown in Fig. 8(b). To allow for a fair comparison we similarly used two grating levels and fixed the period in both the x and y dimensions at 3.1 mm. As in the

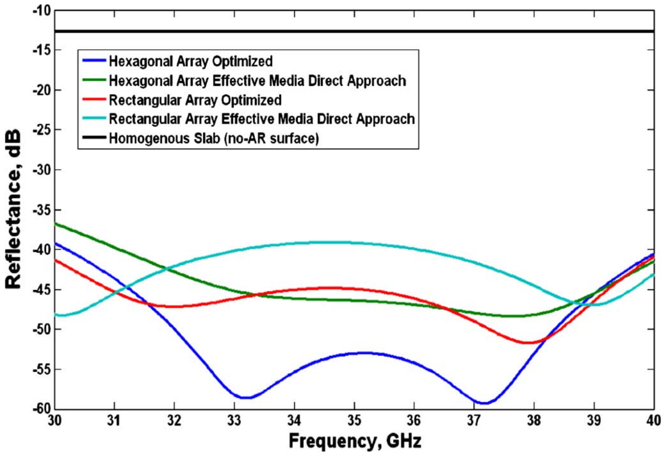

Fig. 9. Simulated results for the AR surfaces of Example #1 using both the hexagonal and rectangular arrays shown in Fig. 8 under normally incident illumination. Plotted is the reflectance in dB as a function of frequency using both the direct (effective media design approach) and the iterative optimization. As a baseline for comparison also presented is the reflected intensity coefficient when no AR surface is added.

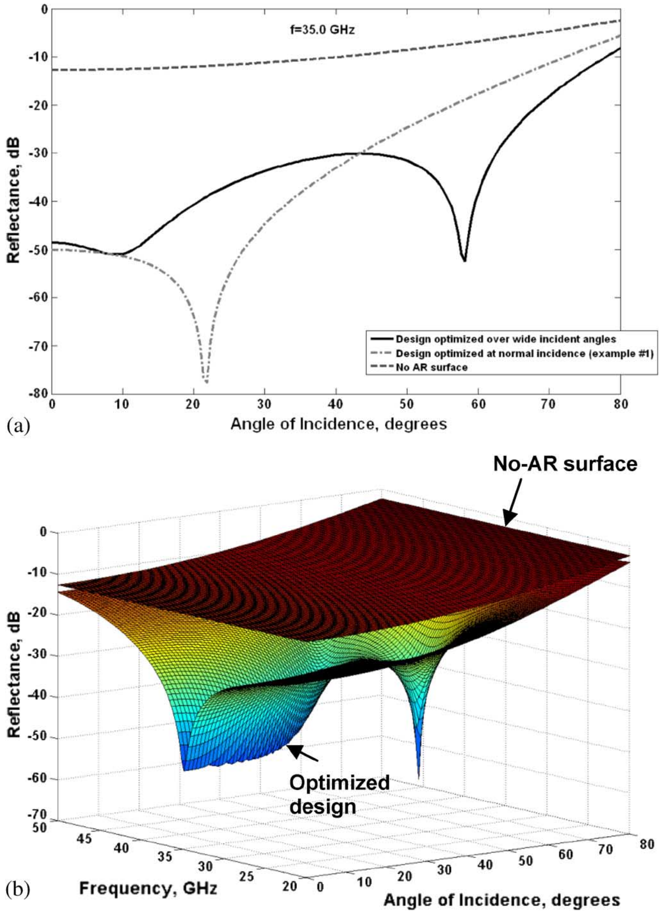

Fig. 10. Simulation results for Example #2 in which an inverse motheye surface was designed to minimize reflected energy over both a wide frequency bandwidth and incident angles for TE polarization. In (a) reflectance is plotted as a function of incident angle at the center frequency of 35 GHz. Also plotted is the reflectance for the optimized hexagonal array given in Example #1 (optimized only for normal incidence) and a reference with no AR surface added. In (b) reflectance is plotted as a function of both frequency and incident angle for the optimized motheye surface and a non-patterned surface.

previous case the grating heights, (h_1 and h_2), and hole diameters, (d_1 and d_2), were assumed variable.

For the structures given in Fig. 8 the intensity reflection coefficient or reflectance, $R = |r|^2$, where r denotes the complex reflection coefficient, is plotted as a function of frequency in Fig. 9. As a baseline for comparison also presented in Fig. 9 is the reflectance of a half-space with no AR surface. Clearly the inverse motheye AR surfaces for both rectangular and hexagonal array designs significantly reduced the reflected energy over the entire frequency band of interest (30–40 GHz). In fact, within the band of interest, R never exceeded -30 dB. This is an impressive result considering the relatively high fractional bandwidth (37%).

It is interesting to note that in this example, as well as most of the design problems we attempted, the designs using hexagonal arrays consistently had lower reflectance than the rectangular arrays. This is not too surprising considering that in the hexagonal geometry the holes can be packed much closer together allowing for a higher volume fraction of material to be removed. Consequently, the effective index of refraction of the top layer can more closely approach free-space in the hexagonal

	d_1 (mm)	d_2 (mm)	h_1 (mm)	h_2 (mm)
Hexagonal array : direct design method	3.0	1.75	1.90	1.51
Hexagonal array : optimized design	2.92	1.83	1.87	1.51
Rectangular array : direct design method	3.06	1.94	1.90	1.41
Rectangular array : optimized design	3.0	1.94	1.80	1.45

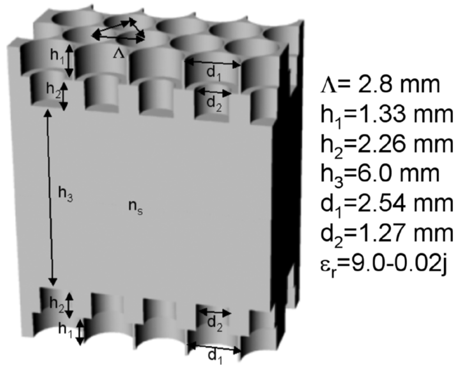

Fig. 11. Inverse motheye AR surface machined on both sides of a Rexolite slab. Designed to be antireflective within the Ka-band (32–38 GHz).

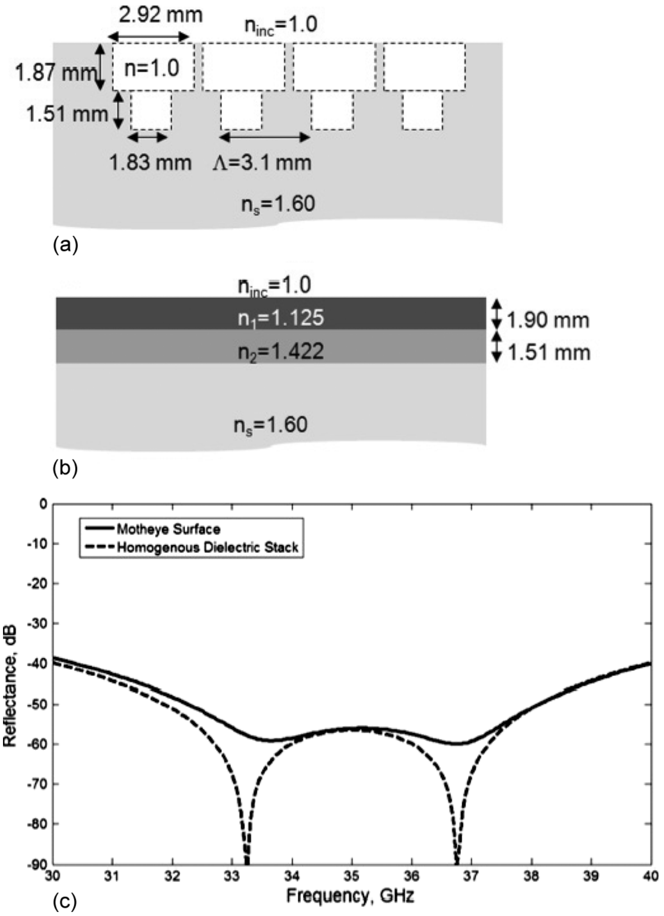

Fig. 12. A numerical comparison between a traditional dielectric stack AR design (12b) and the inverse motheye surface described in Example #1 (12a). The substrate is an infinite half-space of Rexolite ($\varepsilon_{\rm r} = 2.56$). Both structures were designed to be antireflective within the Ka-band (30–40 GHz).

geometry. However, for some applications it might be beneficial to remove less material while still having a reasonably low reflectance. For those applications a rectangular array may be preferred.

B. Example #2: Ka-Band (30–40 GHz) at Wide Incident Angles

In this example an inverse motheye based AR surface was designed to have a low reflectivity over both frequency and angle of incidence. The incident field, as shown in Fig. 3, is assumed to be a TE polarized plane wave incident on the slab at an angle, $\theta_{\rm inc}$. The inverse motheye surface was optimized to create a minimal amount of reflectance over the frequency range 30–40 GHz and incident angles varying from $0 < \theta_{\rm inc} < 60°$. The substrate in which the AR surface would be formed had a dielectric constant of $\varepsilon_{\rm r} = 2.56$, same as the previous example, and was infinitely thick (i.e. half-space). Only the hexagonally packed hole array was used for this example. Similar to the previous example the grating period, Λ, was fixed at 3.1 mm but the grating heights, ($\rm h_1$, and $\rm h_2$), and hole diameters, ($\rm d_1$ and $\rm d_2$), were assumed variable.

The geometry of the optimized structure is identical to that of Fig. 8 with the optimized geometrical parameters provided in the table below. Also provided in the table are the results from the optimization for only normal incidence. The reflectance for these structures is plotted in Fig. 10 as a function of frequency and angle of incidence. The results in Fig. 10 clearly demonstrate how an inverse motheye surface can be used to suppress reflections below −30 dB over incident angles ranging from 0°–60° and a broad frequency band (30–40 GHz). (See the equation at bottom of the page).

	$\rm d_1$ (mm)	$\rm d_2$ (mm)	$\rm h_1$ (mm)	$\rm h_2$ (mm)
Hexagonal array : optimized design for normal incidence only(example#1)	2.92	1.83	1.87	1.51
Hexagonal array : optimized over both frequency and incident angle	3.05	2.21	2.62	1.83

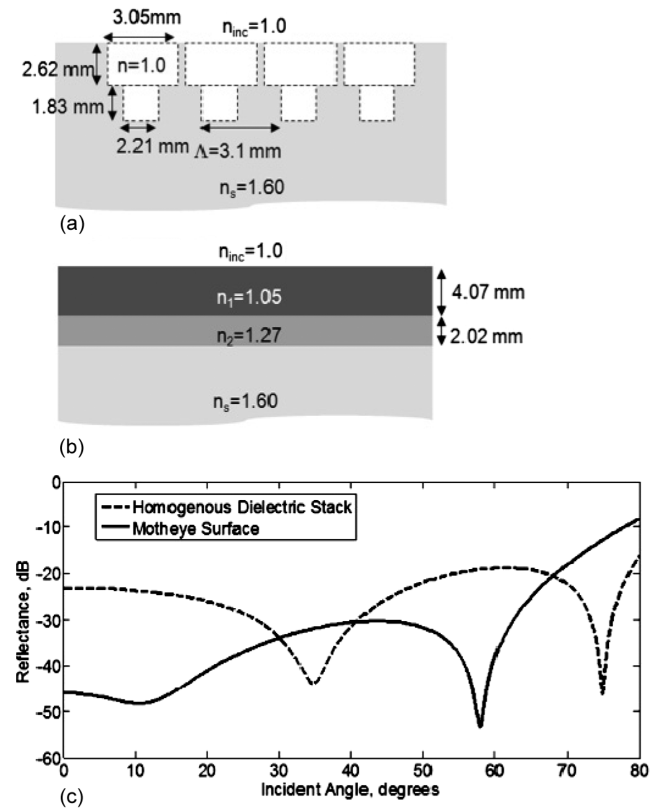

Fig. 13. A numerical comparison between a traditional dielectric stack AR design (13b) and the inverse motheye surface described in Example #2 (13a). The substrate is an infinite half-space of Rexolite ($\varepsilon_r = 2.56$). Both structures were designed to be antireflective within the Ka-band (30–40 GHz) and over incident angles varying from 0–60 degrees. The results shown in Fig. 13(c) are at the center frequency of 35 GHz.

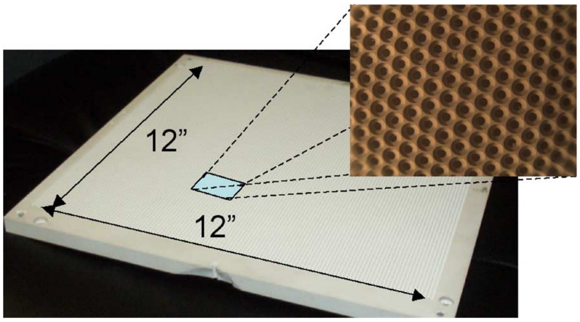

Fig. 14. A $12'' \times 12'' \times 0.5''$ slab of Hik ($\varepsilon_r = 9.0 - 0.02j$) machined to have the hole array structure shown in Fig. 11.

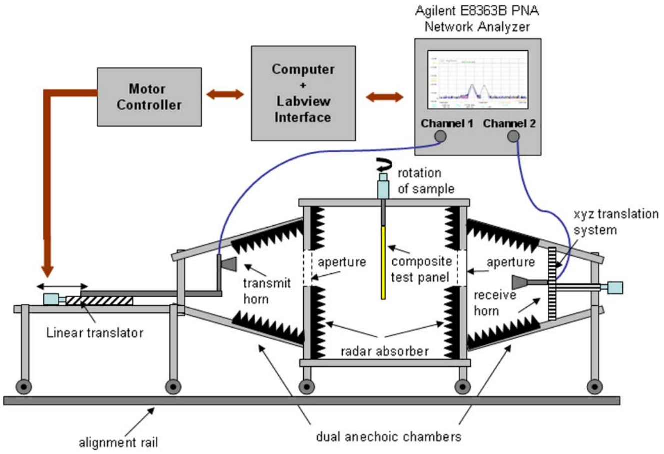

Fig. 15. Experimental system used to measure transmission from the sample shown in Fig. 14.

C. Example #3: Transparent RF Window (Dual AR Surfaces)

In this final example we designed a dielectric slab with an inverse motheye pattern applied to both the top and bottom surfaces, as shown in Fig. 11. The goal was to create a transparent slab (e.g. dielectric RF window) at normal incidence by applying AR surfaces to both the top and bottom surfaces, within the Ka-band (32–38 GHz). We assumed that the substrate in which the AR surface would be formed had a dielectric constant of $\varepsilon_r = 9.0 - 0.02j$ and was 0.5 inch thick. We also employed only a two level grating, as depicted in Fig. 11, with the structure on the top and bottom surfaces being identical. For convenience during fabrication the hole diameters, (d_1 and d_2) were fixed at two conventional drill bit sizes, 0.1 and 0.05 inches respectively. The grating period, Λ, and grating heights, (h_1 and h_2), were assumed variable during the iterative design. Shown in Fig. 11 are the geometrical design results after completion of our iterative design method. The predicted and experimentally measured transmittance, $T = |t|^2$, from this structure is presented in the next section.

D. Comparison of Inverse Moth-Eye Surfaces With a Traditional Dielectric Stack Design

In this section, we provide numerical comparisons between the AR properties of an optimized inverse motheye surface and a traditional dielectric stack. It is worth repeating that the main goal of the inverse motheye design is to create good broadband antireflective properties using known materials and a simple fabrication process (i.e. drilling holes). However, we also hope that the performance will approach that of a traditional AR surface composed of a stack of homogenous dielectrics. To numerically examine this point we looked at the problems described in Examples #1 and #2 and designed dielectric AR stacks using two homogenous dielectric layers to create antireflective behavior over the same frequency band (i.e. Ka-band (30–40 GHz) normal incidence).

For the structure described in Example #1 (see Fig. 8) we employed Collin's equal ripple algorithm (ERAR) described in a previous section to synthesize a dielectric stack [11]–[14]. It was assumed for this case normally incident plane wave illumination. Fig. 12 presents the simulation results from the inverse motheye surface of Example #1 and a two layer dielectric stack designed over the same spectral band. The substrate, as in Example #1, had a dielectric constant of $\varepsilon_r = 2.56$ and was infinitely thick. The calculated reflectance at normal incidence for both the inverse motheye and dielectric stack are shown in Fig. 12(c). Over the band of interest both designs provided very good AR properties (< -40 dB) however the dielectric stack outperformed the inverse motheye, particularly, near those frequencies in which the reflectance theoretically drops to zero. Due to scattering it is unlikely that any structured surface, such as the inverse motheye, will achieve exactly zero reflectance. It is also interesting to note that the optimization algorithm for the

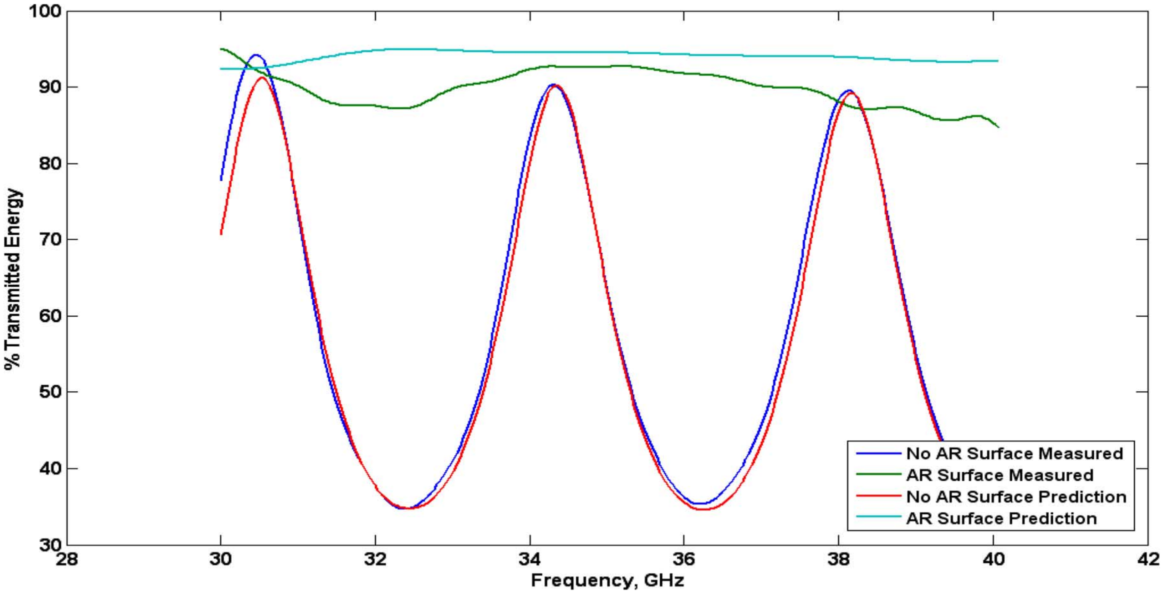

Fig. 16. Simulated and measured %transmitted power at normal incidence for the antireflective sample shown in Fig. 11 and designed in Example #2. Also shown are experimental and predicted results for a reference sample (i.e., no AR surface). Over the design frequency band (32–38 GHz) the AR machined sample transmitted over 86% of the incident power.

inverse motheye surface appears to be driving the effective properties as close to that of a dielectric stack as possible. While we did not quite achieve the performance of the dielectric stack our design was created out of a single substrate with known dielectric properties. Within the Ka-band it would be very difficult to find two materials with exactly the right index of refractions to create the design shown in Fig. 12(b).

In Fig. 13 we provide a similar numerical comparison for the problem described in Example #2. In this case, however, we employed the pattern search optimization algorithm, described earlier in this paper, to optimize the index of refractions and layer thicknesses for each of the two homogenous layers shown in Fig. 13(b) over both frequency (30–40 GHz) and incident angle $(0 < \theta_{\mathrm{inc}} < 60^\circ)$. The results shown in Fig. 13(c) show that in this particular case the inverse motheye surface performed better than the optimized dielectric stack for incident angles below 60 degrees. We speculate that there is an angular dependence to the effective index of the grating layers that helps to reduce reflections at higher these incident angles.

VII. Experimental Validation

To validate the performance of our algorithm experimentally we fabricated the design presented in Example #3 and measured the transmissivity and reflectivity within the Ka-band (30–40 GHz).

The inverse motheye AR surface, shown in Fig. 11, was fabricated from a $12'' \times 12'' \times 0.5''$ plate of high Hik material sold by Emerson & Cuming. We measured the dielectric permittivity of the material to be $\varepsilon_{\mathrm{r}} = 9.0 - 0.02\mathrm{j}$ within the 30–40 GHz band with very little dispersion. The hole array, shown in Fig. 11, were machined into the Hik material using a 3-axis computerized numerical control (CNC) router. The router machined the multi-level hole array on both the top and bottom surfaces of the plate. An image of the fabricated surface is shown in Fig. 14.

To measure the properties of the samples in both transmission and reflection we used the experimental setup shown in Fig. 15. At the heart of this setup is an Agilent PNA Vector Network analyzer with external heads that extend the frequency range from 20 MHz to 110 GHz. On the transmit side a standard gain horn was used to form a quasi-plane wave at the surface of an entrance aperture (8$''$ in diameter). On the receive side an identical standard gain horn was used to detect the transmitted energy through an exit aperture of the same size as the input side. The transmitting horn, input aperture, sample, exit aperture and receive horns are all centered and aligned for maximum transmission of RF energy. The sample was placed on a rotary stage at the center of the chamber to vary the angle of incidence. The entire setup was constructed inside a larger chamber covered with radar absorbing material on all surfaces. Frequency averaging and time-domain gating were used to remove extraneous reflections. In addition the transmit horn is mounted on a linear stage that allows measurements to be taken at different distances to the input aperture. By spatially averaging the results at various transmit locations diffraction effects, due to the finite size of the apertures and samples, can be reduced. This system was modeled after a similar dual anechoic chamber design developed at the Space and Naval Warfare Systems Center (SPAWAR), San Diego CA [17].

A. *Experimental Results at Normal Incidence*

Experimental results for the sample shown in Fig. 14 are presented in Fig. 16 for a normally incident plane wave illumination. Here the measured transmission in %Transmitted Power at normal incidence is plotted as a function of frequency for both the AR machined sample and a reference sample (i.e. Hik plate of the same dimensions but with no AR-surface). Also presented in the figure are the simulated results, using the RCW method, for both samples. The sample machined with the AR inverse motheye surface on both sides transmitted over 86% of

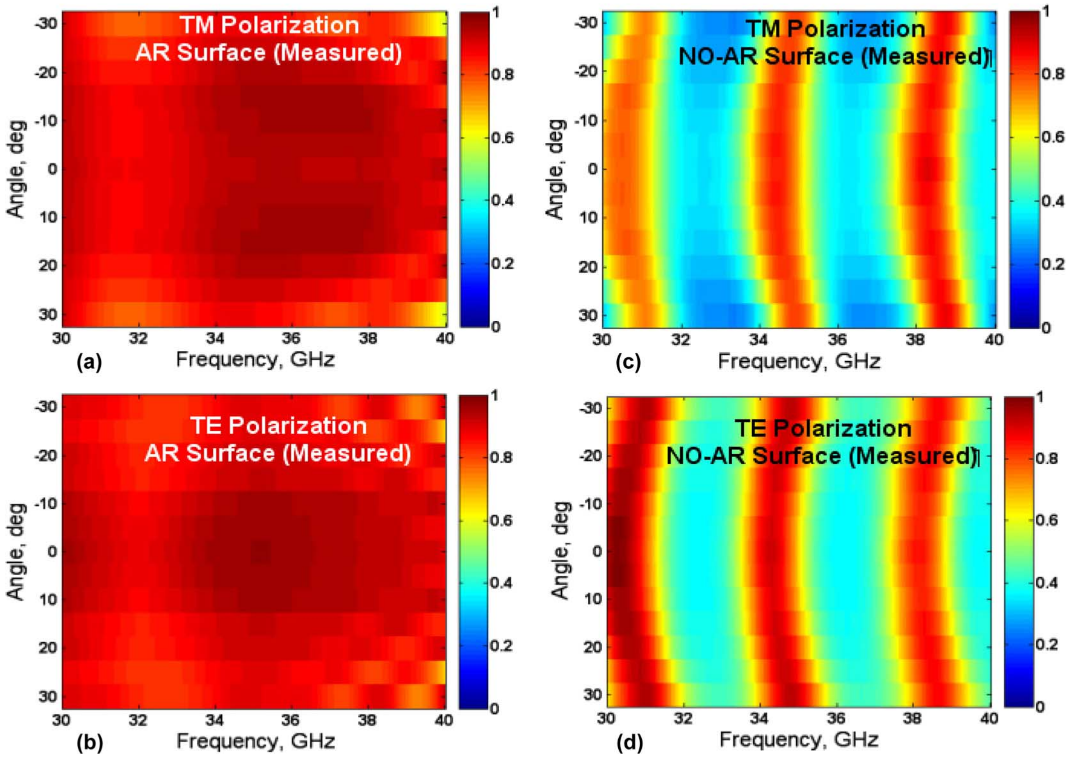

Fig. 17. Measured transmittance as a function of incident angle and frequency for both TE and TM polarizations. Results are given for the AR-machined sample (16a and 16b) and the non-machined reference sample (16c and 16d). Over the design frequency band (32–38 GHz) the AR machined sample transmitted over 80% of the incident power over incident angles of $+ - 30^\circ$ for both TE and TM polarization.

the incident power over the entire 32–38 GHz band. The non-AR machined sample produced the expected standard wave pattern caused by multiple reflections from the two interfaces. There was generally good agreement between the measured and simulated results for both the machined and non-AR machined samples.

B. Experimental Results: Effects of Incident Angle and Polarization

Experimental results are shown in Fig. 17 as a function of frequency, incident angle and polarization for the sample shown in Fig. 14. For these measurements, incident angle was varied by rotating the sample between -30° to $+30^\circ$ with respect to the incoming incident plane wave. Due to the limited size of the samples it was not possible to test incident angles much greater than 30°. For each incident angle measurements were made for both TE and TM polarization. Measurements were acquired within the 30–40 GHz band for both the AR machined sample (Fig. 14) and the non-machined reference sample.

Referring to Fig. 17 it is interesting to note that even though this sample was designed and optimized to be non-reflective only for normally incident illumination it still transmitted over 80% of the incident power over the entire range of incident angles (e.g., -30° to $+30^\circ$) within the designed frequency band of 32–38 GHz. This was true for both TE and TM polarization. It was not surprising that for the non-machined reference sample the transmitted power was highly dependent on the frequency and, to a lesser extent, the angle of incidence and polarization.

VIII. DISCUSSION AND CONCLUSION

In this paper we presented a method for creating broadband anti-reflective surfaces using subwavelength arrays of holes drilled into a lossless dielectric. Analogous to motheye type AR surfaces used primarily at optical frequencies we refer to this geometry as inverse motheye surfaces. Both a direct design approach, using effective media theory, and an iterative optimization algorithm were described. Several design examples were presented that demonstrated the inverse motheye surface's ability to minimize reflections over a broadband of frequencies and incident angles. One of the design examples was experimentally fabricated and characterized for validation.

REFERENCES

[1] L. Yujiri, M. Shoucri, and P. Moffa, "Passive millimeter wave imaging," *IEEE Microwave Mag.*, vol. 4, no. 3, pp. 39–50, Sept. 2003.
[2] R. Appleby and R. N. Anderton, "Millimeter-wave and submillimeter-wave imaging for security and surveillance," *Proc. IEEE*, vol. 95, pp. 1683–1690, Aug. 2007.
[3] D. A. Wikner and G. Samples, "Polarimetric passive millimeter-wave sensing," in *SPIE Proc. Passive Millimeter-Wave Imaging Technology*, 2001, vol. 4373, pp. 86–93.
[4] J. Santos and L. Bernado, "Antireflective structures with use of multilevel subwavelength zero-order gratings," *Appl. Opt.*, vol. 36, no. 34, pp. 8935–8938, Dec. 1997.
[5] R. Brauer and O. Bryngdahl, "Design of antireflective gratings with approximate and rigorous methods," *Appl. Opt.*, vol. 33, no. 34, pp. 7875–7882, Dec. 1994.
[6] M. Shokooh-Saremi and M. Mirsalehi, "Comparison of antireflective surfaces based on two-dimensional binary gratings and thin-film coatings," *Appl. Opt.*, vol. 44, no. 19, pp. 3877–3884, Jul. 2005.
[7] P. Lalanne and J. Hugonin, "High-order effective-medium theory of subwavelength gratings in classical mounting: Application to volume holograms," *J. Opt. Soc. Am. A*, vol. 15, pp. 1843–1851, 1998.

[8] M. G. Moharam and T. K. Gaylord, "Rigorous coupled-wave analysis of planar-grating diffraction," *J. Opt. Soc. Am. A*, vol. 71, pp. 811–818, 1981.

[9] M. G. Moharam, E. B. Grann, D. A. Pommet, and T. K. Gaylord, "Formulation for stable and efficient implementation of the rigorous coupled wave analysis of binary gratings," *J. Opt. Soc. Am. A*, vol. 12, pp. 1068–1076, 1995.

[10] M. G. Moharam, D. A. Pommet, and E. B. Grann, "Stable implementation of the rigorous coupled-wave analysis for surface relief gratings: Enhanced transmittance matrix approach," *J. Opt. Soc. Am. A*, vol. 12, pp. 1077–1086, 1995.

[11] P. Lalanne, "Improved formulation of the coupled-wave method for two-dimensional gratings," *J. Opt. Soc. Am. A*, vol. 14, pp. 1592–1598, 1997.

[12] E. Noponen and J. Turunen, "Eigenmode method for electromagnetic synthesis of diffractive element with three-dimensional profiles," *J. Opt. Soc. Am. A*, vol. 11, pp. 2494–2502, 1994.

[13] R. E. Collin, *Foundations of Microwave Engineering*. New York: McGraw-Hill, 1966.

[14] R. E. Collin, "Theory and design of wide-band multisection quarter-wave transformers," *Proc. IRE*, vol. 43, pp. 179–185, 1955.

[15] L. Young, "Synthesis of multiple antireflective films over a prescribed frequency band," *J. Opt Soc. Am.*, vol. 51, pp. 967–974, 1961.

[16] H. J. Riblet, "General synthesis of quarter-wave impedance transformers," *IRE Trans. Microw. Theory Tech.*, vol. MTT-5, pp. 36–43, Jan. 1957.

[17] J. H. Meloling, W. M. Massey, and D. E. Hurdsman, "Dual-Chambered anechoic chamber and method for making transmission measurements using spatial averaging," U.S. patent 6,842,013.

Mark S. Mirotznik (S'87–A'93) received the B.S.E.E. degree from Bradley University, Peoria, IL, in 1988 and the M.S.E.E. and Ph.D. degrees from the University of Pennsylvania, Philadelphia, in 1991 and 1992, respectively.

From 1992 to 2009, he was a faculty member in the Department of Electrical Engineering, The Catholic University of America, Washington, DC. Since 2009, he is an Associate Professor and Director of Educational Outreach in the Department of Electrical and Computer Engineering, University of Delaware, Newark. In addition to his academic positions he an Associate Editor of the *Journal of Optical Engineering* and also holds the position of Senior Research Engineer for the Carderock Division, Naval Surface Warfare Center, West Bethesda, MD. His research interests include applied electromagnetics and photonics, computational electromagnetics and bioelectromagnetics.

Brandon L. Good (M'09) received the B.A. and M.S. degree in electrical engineering from The Catholic University of America, Washington, DC, in 2009. He is currently working toward the Ph.D. degree at the University of Delaware, Newark.

Currently, he is a Junior Engineer at the Carderock Division, Naval Surface Warfare Center, West Bethesda, MD. His research interests include meta-material design and fabrication and advanced material measurement techniques.

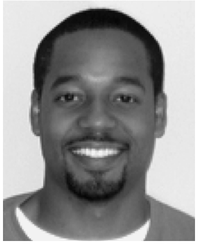

Paul Ransom (M'09) received the B.S.E.E. degree from Southern University, Baton Rouge, LA and the M.S.E.C.E. degree from the Georgia Institute of Technology, Atlanta. He is currently working toward the Ph.D. degree at the Catholic University of America, Washington, DC.

He is currently a Senior Research Engineer a the Carderock Division, Naval Surface Warfare Center, West Bethesda, MD. His research interest include computational electromagnetics and electromagnetically engineered materials.

David Wikner received the B.A. degree in physics and mathematics from Ohio Wesleyan University, Delaware, in 1986 and the M.S. degree in physics from Stanford University, Stanford, CA, in 1988.

In 1988, he joined the U.S. Army Research Laboratory, Adelphi, MD, where he currently leads the Millimeter Wave (MMW) Sensor Technology Team. He and his group explore MMW imaging phenomenology, system designs, and novel device technology. He has worked extensively with 94-GHz radar systems for vehicle and ground clutter measurements. For over 15 years he has been involved in the study of MMW imaging technology. The last several years his work has focused on efforts to create affordable MMW imaging systems for Army applications using new device technology and quasi-optical signal processing techniques.

Mr. Wikner and has been a Chair of the SPIE Passive Millimeter-Wave Imaging Technology Conference since 2002.

Joseph N. Mait (S'78–M'84–SM'03) received the B.S.E.E. degree from the University of Virginia, Charlottesville, in 1979 and the M.S.E.E. and Ph.D. degrees from the Georgia Institute of Technology, Atlanta, in 1980 and 1985, respectively.

Since 1989, he has been with the U.S. Army Research Laboratory, Adelphi, MD, where he is currently Senior Technical Researcher for electromagnetics. Previously, he was an Assistant Professor of electrical engineering at the University of Virginia, from 1984 to 1989, and an Adjunct Associate Professor at the University of Maryland, College Park, from 1997 to 2005. He has also held visiting positions at the Lehrstuhl fur Angewandte Optik, Universitat Erlangen-Nurnberg, Germany, and the Center for Technology and National Security Policy, National Defense University, Washington, DC. His research interests include the application of optics, photonics, and electromagnetics to sensing and sensor signal processing.

Dr. Mait is a Fellow of SPIE and OSA.